

# Multi-Modal Environment-Aware Beam Management for Massive MIMO: A Geometry-Driven Virtual Base Station Framework

Yijie Bian, Wei Guo, *Member, IEEE*, Jie Yang, *Member, IEEE*, Shenghui Song, *Senior Member, IEEE*,  
Jun Zhang, *Fellow, IEEE*, Shi Jin, *Fellow, IEEE*, Khaled B. Letaief, *Fellow, IEEE*

**Abstract**—High-frequency massive multiple-input multiple-output (MIMO) systems promise ultra-high data rates. However, efficient beam management remains challenging due to the prohibitive beam training overhead and intricate coordination required in multi-user MIMO (MU-MIMO) scenarios. To address these bottlenecks, environment-aware communications have emerged as a promising paradigm, leveraging site-specific knowledge to circumvent exhaustive pilot-based beam training and streamline multi-user communications. In this paper, we propose an interpretable and geometry-driven framework that utilizes multi-modal environmental data, specifically regional 3D light detection and ranging (LiDAR) point clouds and location information, to construct an offline virtual base station (VBS) database. By modeling dominant reflection paths via mirror symmetry across building facades reconstructed from the point clouds, the VBS database provides a compact and sparse description of the wireless propagation environment. To bridge the semantic gap between geometric information and wireless channels, we develop a coarse channel reconstruction mechanism that estimates channel parameters directly from VBS-derived geometric relationships. Based on the resulting coarse beamspace representation, we design a VBS-assisted orthogonal-pilot (VOP)-based partial beam training scheme to refine the coarse estimates with minimal online training overhead. Finally, to tackle the combinatorial beam selection problem and manage inter-user interference, we propose a hierarchical deep reinforcement learning framework, namely a dual-agent dueling double deep Q-network, for coordinated beam selection (DD3QN-CBS). Simulation results demonstrate consistent gains in both beam training efficiency and beam selection performance over heuristic and learning-based baselines.

**Index Terms**—Virtual base station, MU-MIMO beam management, multi-modal data, deep reinforcement learning

## I. INTRODUCTION

To meet the exponential growth in data traffic and throughput requirements of the sixth-generation (6G) networks, exploring spectrum resources at increasingly elevated frequencies has become imperative [2]. High-frequency bands, ranging from millimeter-wave (mmWave) to sub-terahertz (sub-THz) and terahertz (THz), are poised to serve as cornerstones of future wireless systems. These bands offer ultra-high bandwidths capable of supporting massive data throughput and enhanced connectivity, thereby enabling advanced applications in both outdoor and indoor scenarios, such as holographic

telepresence and immersive extended reality [2]. However, these high-frequency bands suffer from high blockage sensitivity, low diffraction capability, and increased propagation attenuation. To compensate for this attenuation, massive multiple-input multiple-output (MIMO) technology employing large-scale antenna arrays has been widely adopted. By leveraging high array gains through beamforming and spatial multiplexing, massive MIMO systems can significantly enhance link reliability and spectral efficiency [3], [4].

Nevertheless, realizing the full potential of massive MIMO in high-frequency bands presents significant challenges. Due to hardware cost and power consumption constraints, transceivers typically adopt analog or hybrid architectures in which the number of radio frequency (RF) chains is much smaller than that of antenna elements. Such hardware constraints restrict the system to low-dimensional observations, making it computationally intensive and time-prohibitive to acquire accurate high-dimensional channel state information (CSI) in real time. Consequently, practical standards and existing studies resort to codebook-based beam management [5], [6]. Instead of conducting explicit channel estimation, the base station (BS) and user select the optimal beam pair from predefined codebooks through beam training. While feasible, this approach introduces a critical bottleneck that exhaustive beam training incurs substantial overhead and latency [7]. The challenge becomes even more pronounced in multi-user scenarios, where the network must coordinate beam selection across users to mitigate inter-user interference, leading to a combinatorial search over beam pairs [8].

### A. Prior Works and Limitations

To address the prohibitively high overhead of acquiring real-time CSI for beam management, a promising strategy is to exploit environmental sensing data, such as light detection and ranging (LiDAR) point clouds [9], [10], radio detection and ranging (Radar) images [11], and red-green-blue (RGB) images [12]. Since wireless propagation characteristics are tightly coupled with the surrounding physical environment [13], such sensing data can be used to predict beam index distributions and further prune the beam search space.

Early research on multi-modal sensing-aided beam management primarily targeted single-user scenarios. For instance, Feng *et al.* [13] developed a pre-training and transfer-learning strategy to predict the optimal beam from ambient environmental information. Yang *et al.* [14] proposed an environment-semantics network to predict the optimal beam index and blockage state. Bian *et al.* [15] incorporated 3D LiDAR point clouds and location data to assist beam tracking in vehicle-to-vehicle line-of-sight (LoS) scenarios. However, LoS-oriented sensors such as cameras struggle in non-line-of-

An earlier version of this paper was presented in part at the IEEE Wireless Communications and Networking Conference (WCNC), Kuala Lumpur, Malaysia, in April 2026 [1].

Y. Bian, W. Guo, S. Song, J. Zhang, and K. B. Letaief are with the Department of Electronic and Computer Engineering, Hong Kong University of Science and Technology, Hong Kong SAR. Emails: ybianaf@connect.ust.hk, {eewei@guo, eeshsong, eejzhang, eekhaled}@ust.hk.

J. Yang is with the School of Automation, Southeast University, Nanjing, China. Email: yangjie@seu.edu.cn.

S. Jin is with the School of Information Science and Engineering, Southeast University, Nanjing, China. Email: jinshi@seu.edu.cn.

sight (NLoS) conditions, and therefore data-driven methods based only on LoS information may fail to capture dominant NLoS paths in urban environments.

Although multi-modal sensing has been widely studied for single-user beam management, its extension to multi-user scenarios remains underexplored. Directly transferring single-user sensing-aided methods to multi-user contexts often leads to severe performance degradation because of inter-user interference. Recently, a few works have attempted to bridge this gap. For example, Ahn *et al.* [16] employed two serial deep neural networks for joint user and beam selection using captured image data, but only in LoS scenarios. Kartik *et al.* [17] proposed a deep learning (DL) based channel estimation framework that reconstructed the complete beamspace channel using sensing data, assuming unlimited phase-shifter resolution. Nevertheless, such a framework also incurred high computational overhead because it processed raw multi-modal data. Mohammad *et al.* [18] used contextual integrated sensing and communication (ISAC) data together with a multi-modal transformer encoder for beam selection based on deep reinforcement learning (DRL). However, inter-user interference is not explicitly considered because the evaluated user distribution is sparse. Moreover, existing sensing-assisted methods often entangle multi-modal feature extraction and multi-user coordination within a unified black-box network. Since the algebraic patterns of inter-user interference are inherently decoupled from environmental geometry, this methodological entanglement can lack structural interpretability and limit scalability.

### B. Main Contributions

To overcome the limitations of existing methods, we shift the focus from black-box mapping to explicit geometric abstraction. Rather than treating multi-modal environmental data as generic input features, we use them to extract site-specific propagation structures that can be organized into interpretable geometric priors for beam management. By exploiting site-specific propagation invariants, we develop a framework that maps raw multi-modal data into a structured database of virtual base stations (VBSs). Serving as virtual mirror images of the physical BS across major reflective facades, these VBSs convert environmental geometry into beamspace priors for interference-aware MU-MIMO beam management. Specifically, the main contributions of this study are summarized as follows:

- We introduce a VBS construction scheme that converts environmental data into a sparse and interpretable radio propagation representation. Specifically, the proposed scheme extracts dominant reflective surfaces from 3D LiDAR point clouds and the BS location to generate VBSs as virtual images of the physical BS without preliminary wireless measurements. By integrating VBS locations with LoS and virtual line-of-sight (VLoS) coverage regions, the resulting database provides a compact, site-specific description of dominant propagation paths with low storage overhead.
- Since the VBS database provides only a coarse beamspace prior, online calibration is required to account for residual geometric uncertainty and propagation variations. To this end, we propose the VBS-assisted orthogonal-pilot (VOP)-based partial beam train-

ing scheme, supported by the physics-compliant coarse channel reconstruction. The scheme infers beam-relevant parameters from geometric relationships, thereby bridging environmental geometry and online beam training while reducing the beam training overhead.

- After partial beam training, the remaining challenge is to coordinate beam selection among multiple users under inter-user interference. We therefore propose a dual-agent dueling double deep Q-network for coordinated beam selection (DD3QN-CBS), which exploits complementary beamspace features from both the VBS-assisted coarse representation and the refined online measurements. Under a hierarchical leader-follower architecture, the BS-side and user-side agents sequentially determine their beam selection actions. Moreover, an online action masking mechanism is embedded in the BS-side agent to structurally suppress inter-user interference, accelerate training convergence, and improve beam selection performance.

The remainder of the paper is organized as follows. Section II presents the downlink MU-MIMO beam selection problem formulation and motivates the VBS abstraction from mmWave propagation characteristics. Section III describes the offline VBS database construction from multi-modal data. Section IV develops the VBS-guided beam management framework, comprising coarse channel reconstruction, a VOP-based partial beam training scheme, and a DD3QN-CBS framework and implementation. Section V presents evaluations on realistic urban layouts and comparisons with baseline strategies. Section VI concludes the work.

## II. SYSTEM MODEL AND FRAMEWORK MOTIVATION

This section establishes the system-level foundation for the proposed framework. We first formulate the downlink MU-MIMO beam selection problem. Based on this general formulation, we then motivate the VBS abstraction as a geometry-driven representation that connects high-frequency propagation characteristics with the subsequent VBS-guided beam management pipeline.

### A. Beam Selection Problem Formulation

We consider a downlink MU-MIMO system where the BS is equipped with a hybrid beamforming architecture consisting of  $N_{\text{BS}}$  transmit uniform linear array (ULA) antennas and  $N_{\text{RF}}$  RF chains, serving  $K$  co-scheduled users. Each user is equipped with  $N_{\text{UE}}$  receive ULA antennas and an analog combining architecture. The BS applies an analog precoder  $\mathbf{F}_{\text{RF}} = [\mathbf{f}_{\text{RF}}^1, \mathbf{f}_{\text{RF}}^2, \dots, \mathbf{f}_{\text{RF}}^{N_{\text{RF}}}] \in \mathbb{C}^{N_{\text{BS}} \times N_{\text{RF}}}$  and a digital baseband precoder  $\mathbf{F}_{\text{BB}} = [\mathbf{f}_{\text{BB}}^1, \mathbf{f}_{\text{BB}}^2, \dots, \mathbf{f}_{\text{BB}}^K] \in \mathbb{C}^{N_{\text{RF}} \times K}$ . The  $k$ -th user employs an analog combining vector  $\mathbf{w}_k \in \mathbb{C}^{N_{\text{UE}} \times 1}$ , and the wireless channel from the BS to this user is denoted by  $\mathbf{H}_k \in \mathbb{C}^{N_{\text{UE}} \times N_{\text{BS}}}$ .

Let  $\mathbf{s} = [s_1, \dots, s_K]^T$  be the transmitted symbol vector with  $\mathbb{E}[\mathbf{s}\mathbf{s}^H] = \mathbf{I}_K$ . The post-combining received signal at the  $k$ -th user is expressed as

$$y_k = \mathbf{w}_k^H \mathbf{H}_k \mathbf{F}_{\text{RF}} \mathbf{f}_{\text{BB}}^k s_k + \sum_{j \neq k} \mathbf{w}_k^H \mathbf{H}_k \mathbf{F}_{\text{RF}} \mathbf{f}_{\text{BB}}^j s_j + n_k, \quad (1)$$

where  $n_k \sim \mathcal{CN}(0, N_0 W)$  represents the additive white Gaussian noise, with  $N_0$  and  $W$  denoting the noise power spectral density and the system bandwidth, respectively. Accordingly,

the downlink signal-to-interference-plus-noise ratio (SINR) is given by

$$\text{SINR}_k = \frac{|\mathbf{w}_k^H \mathbf{H}_k \mathbf{F}_{\text{RF}} \mathbf{f}_{\text{BB}}^k|^2}{\sum_{j \neq k} |\mathbf{w}_k^H \mathbf{H}_k \mathbf{F}_{\text{RF}} \mathbf{f}_{\text{BB}}^j|^2 + N_0 W}. \quad (2)$$

To incorporate quality of service (QoS) constraints, the system effective spectral efficiency (ESE) is evaluated by penalizing users failing an SINR threshold  $\text{SINR}_{\text{thres}}$  via an indicator function  $\mathbb{I}(\cdot)$ , which is defined as

$$\text{ESE} = \sum_{k=1}^K \log_2 (1 + \text{SINR}_k) \cdot \mathbb{I}(\text{SINR}_k \geq \text{SINR}_{\text{thres}}). \quad (3)$$

The joint analog and digital beam selection problem maximizing the system ESE is formulated as

$$\max_{\mathbf{F}_{\text{RF}}, \{\mathbf{w}_k\}_{k=1}^K, \mathbf{F}_{\text{BB}}} \text{ESE} \quad (4a)$$

$$\text{s.t.} \quad \mathbf{f}_{\text{RF}}^i \in \mathcal{F}_{\text{BS}}, \quad i = 1, \dots, N_{\text{RF}}, \quad (4b)$$

$$\mathbf{w}_k \in \mathcal{W}_{\text{UE}}, \quad k = 1, \dots, K, \quad (4c)$$

$$\text{Tr}(\mathbf{F}_{\text{RF}} \mathbf{F}_{\text{BB}} \mathbf{F}_{\text{BB}}^H \mathbf{F}_{\text{RF}}^H) \leq P_{\text{T}}, \quad (4d)$$

where  $\mathcal{F}_{\text{BS}}$  and  $\mathcal{W}_{\text{UE}}$  denote the discrete Fourier transform (DFT) analog beam codebooks at the BS and users, respectively, and  $P_{\text{T}}$  represents the total transmit power budget. Assuming a standard half-wavelength antenna spacing, the array response vector  $\mathbf{a}(\theta; N) \in \mathbb{C}^{N \times 1}$  for an  $N$ -element ULA is defined as

$$\mathbf{a}(\theta; N) \triangleq \frac{1}{\sqrt{N}} [1, e^{j\pi\theta}, \dots, e^{j\pi(N-1)\theta}]^T. \quad (5)$$

Based on (5), the analog beamforming codebooks  $\mathcal{F}_{\text{BS}}$  and  $\mathcal{W}_{\text{UE}}$  are constructed by uniformly quantizing the spatial frequency domain as

$$\mathcal{F}_{\text{BS}} \triangleq \left\{ \mathbf{a} \left( \frac{2m-1-N_{\text{BS}}}{N_{\text{BS}}}; N_{\text{BS}} \right) \mid m = 1, \dots, N_{\text{BS}} \right\}, \quad (6)$$

$$\mathcal{W}_{\text{UE}} \triangleq \left\{ \mathbf{a} \left( \frac{2n-1-N_{\text{UE}}}{N_{\text{UE}}}; N_{\text{UE}} \right) \mid n = 1, \dots, N_{\text{UE}} \right\}. \quad (7)$$

In problem (4), the physical implications of the mathematical objectives and hardware limitations are detailed as follows. The objective (4a) targets the maximization of the system ESE. Constraints (4b) and (4c) mathematically confine the continuous search space to the discrete grids mandated by the analog phase shifter hardware resolutions. Finally, constraint (4d) accounts for the total power budget limitations. To decouple this joint combinatorial optimization tractably, the analog beamforming matrices  $\mathbf{F}_{\text{RF}}$  and  $\{\mathbf{w}_k\}_{k=1}^K$  are first dynamically selected from the finite codebook spaces, after which the digital precoder  $\mathbf{F}_{\text{BB}}$  can be optimized conditioned on the low-dimensional effective channel matrix.

The primary challenge in solving (4) stems from the excessive training overhead required to acquire full CSI, coupled with the combinatorial complexity of optimizing MU-MIMO joint beam pairs. This bottleneck motivates the use of stable environmental priors that can reduce the dependence on exhaustive wireless measurements before online beam

selection.

### B. Concept Generation and Formulation of VBS

As shown in Fig. 1(a), wireless communication systems operating at high frequencies, such as mmWave, face significant path attenuation and severe blockage loss, which frequently prevent direct LoS paths from providing reliable coverage. Under these conditions, large and static building facades can act as persistent specular reflectors that create stable auxiliary propagation paths. This geometric property motivates the construction of VBSs to represent reflected links in an interpretable form.

Formally, for a given reflecting facade, the corresponding VBS is defined as the mirror image of the physical BS with respect to that facade. Each VBS therefore represents a single-bounce reflection path between the BS and user through the associated reflector.<sup>1</sup> The proposed VBS concept generalizes the geometric principles of virtual anchor points [21] to environment-aware beam management. While virtual anchors are typically used as low-dimensional geometric beacons for positioning, VBSs act as virtual mirror images of the physical BS and encode site-specific reflection opportunities for environment-aware beam management.

This single-bounce VBS abstraction is consistent with high-frequency urban propagation. In contrast to ground reflections [22], which are highly susceptible to dynamic moving occlusions, facade-induced virtual links offer structural permanence. Therefore, the VBSs considered in this paper provide a compact geometric basis for the subsequent MU-MIMO beam selection.

To make this geometric abstraction directly usable for beam management, we define a VBS database, as shown in Fig. 1(b1) and Fig. 1(b2), that stores the VBS locations and their quantized coverage regions. Specifically, the  $v$ -th VBS is characterized by its location  $\mathbf{o}_{\text{VBS}}^v$  and its VLoS coverage region  $\mathcal{C}_v$  for  $v \geq 1$ . For notational consistency,  $\mathcal{C}_0$  denotes the LoS coverage region of the physical BS. Together, the physical BS, the VBS locations, and the coverage regions  $\{\mathcal{C}_v\}_{v \geq 0}$  transform environmental geometry into path availability and angular priors. As depicted in Fig. 1(c), these geometric insights are particularly valuable for MU-MIMO beam management, where stable VLoS paths can serve as auxiliary links to spatially separate co-scheduled users and mitigate inter-user interference. In the following section, we present the methodology for constructing the VBS database.

## III. VBS DATABASE CONSTRUCTION FROM MULTI-MODAL DATA

This section develops the offline construction procedure for the compact VBS database without wireless measurements. As depicted in Fig. 2, the process comprises four main stages: 3D LiDAR point cloud acquisition, geometric information extraction, VBS location computation, and coverage computation and storage.

### A. Geometric Information Extraction

To extract major reflective facades, we first segment the static point cloud into individual building objects, thereby

<sup>1</sup>The single-bounce assumption is consistent with mmWave channel observations, where dominant NLoS components are mainly produced by single-bounce reflections, while multi-bounce paths experience compounded reflection loss and usually carry negligible energy [19], [20].

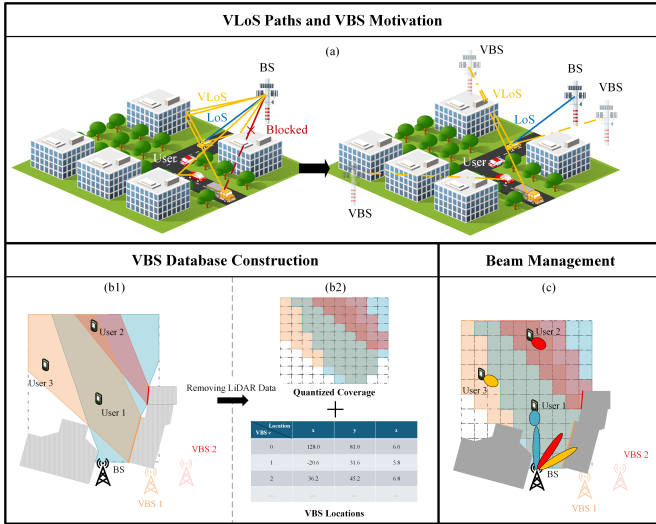


Fig. 1: VBS motivation and application. (a) Building facades can generate dominant VLoS paths through single-bounce reflections when the LoS path is blocked. (b1) The VLoS coverage area can extend the effective communication area to alleviate the LoS outage problem. (b2) Constructed VBS locations and quantized coverage regions form a compact environmental abstraction where the original 3D LiDAR point clouds can be removed. (c) The resulting VBS information can support environment-aware MU-MIMO beam selection by providing spatially distinct VLoS links.

constraining surface reconstruction to geometrically coherent structural regions. To this end, these static scene objects are segmented into distinct clusters using the density-based spatial clustering of applications with noise (DBSCAN) algorithm [23]. For the  $m$ -th segmented object, a set of  $N_m$  triangular meshes is generated using surface reconstruction [24] and surface simplification [25]. For the  $i$ -th triangular mesh  $\mathcal{T}_i$ , the outer normal vector  $\mathbf{g}_i \in \mathbb{R}^{3 \times 1}$  is computed from its three edge vectors  $\mathbf{e}_i^k \in \mathbb{R}^{3 \times 1}$  ( $k = 1, 2, 3$ ), which are derived from adjacent vertex locations  $\mathbf{v}_i^k \in \mathbb{R}^{3 \times 1}$ . The centroid is calculated as  $\mathbf{v}_i^c = \frac{1}{3} \sum_{k=1}^3 \mathbf{v}_i^k \in \mathbb{R}^{3 \times 1}$ . These vertices and the normal vector geometrically define the  $i$ -th triangular mesh.

While a complete facade may not be perfectly smooth, its constituent meshes can be treated as independent reflectors. Once the reflector geometry has been extracted, the mirror principle can be applied to obtain the locations of VBSs from valid facades.

### B. Determination of VBS Locations

Based on the extracted triangular meshes, the location of a candidate VBS can be computed by mirroring the BS with respect to the plane of each mesh. However, not every candidate VBS obtained in this manner corresponds to a physically realizable reflection path. Some meshes may be improperly oriented with respect to the BS, while others may be blocked by surrounding objects. Therefore, before computing and retaining the corresponding VBS locations, we need to identify valid meshes that satisfy two fundamental geometric conditions: the orientation condition and the unobstructed path condition.

The orientation condition ensures that the mesh is oriented toward the BS, which is a prerequisite for reflection. Let  $\mathbf{p}_i^c = \mathbf{v}_i^c - \mathbf{o}_{BS}$  denote the vector from the BS to the mesh centroid. The condition is expressed as

$$\mathbf{g}_i^T \mathbf{p}_i^c > 0, \quad (8)$$

implying the angle between  $\mathbf{g}_i$  and  $\mathbf{p}_i^c$  is less than  $\pi/2$ , i.e., the mesh faces the BS.

The unobstructed path condition evaluates whether the target mesh is visible from the BS. For each triangular mesh  $\mathcal{T}_i$ , we examine the visibility of its three vertices from the BS. A vertex is regarded as visible if the line segment connecting it to the BS is not occluded by any other mesh in the reconstructed environment. To mathematically represent this visibility test, we define an indicator function  $\text{Intersect}(\mathbf{o}_{BS}, \mathbf{v}_i^k, \mathcal{T}_j)$ , which equals 1 if mesh  $\mathcal{T}_j$  intersects the visibility segment from  $\mathbf{o}_{BS}$  to  $\mathbf{v}_i^k$ , and 0 otherwise. In practice, this indicator is evaluated using the Möller-Trumbore ray-triangle intersection algorithm [26]. Then,  $\mathcal{T}_i$  satisfies the unobstructed path condition if at least one of its vertices is visible from the BS, i.e.,

$$\sum_{j \neq i} \text{Intersect}(\mathbf{o}_{BS}, \mathbf{v}_i^k, \mathcal{T}_j) = 0, \quad \exists k \in \{1, 2, 3\}. \quad (9)$$

This condition indicates that the candidate reflector has at least one unobstructed incident path from the BS.

Upon satisfying these conditions, the VBS generated by the  $i$ -th mesh is computed as the mirror image of the BS location, which can be expressed as

$$\tilde{\mathbf{o}}_{VBS}^i = \mathbf{o}_{BS} - 2d_i \mathbf{g}_i, \quad (10)$$

where  $\tilde{\mathbf{o}}_{VBS}^i$  is the original location of the  $i$ -th VBS, and  $d_i$  is the distance from the BS to the  $i$ -th mesh plane.

In practice, LiDAR measurement noise and surface reconstruction deviations may cause multiple meshes associated with the same physical facade to generate numerous slightly displaced raw VBSs. To resolve this data redundancy, our primary objective is to replace these redundant raw VBS coordinates with a compact set of database representatives. To this end, we apply hierarchical density-based spatial clustering of applications with noise (HDBSCAN) [27] to the coordinates of all valid raw VBSs. Specifically, for the  $v$ -th cluster detected, its representative VBS location,  $\mathbf{o}_{VBS}^v$ , is computed as the cluster centroid, while its associated meshes are defined as the union of meshes corresponding to all constituent raw VBSs within that cluster. As conceptualized in Fig. 2(c), this cluster center is extracted by averaging multiple slightly displaced raw VBS locations, e.g.,  $\tilde{\mathbf{o}}_{VBS}^{v_1}$  and  $\tilde{\mathbf{o}}_{VBS}^{v_2}$  generated by constituent meshes of the same facade. Compared with standard DBSCAN, which can be sensitive to highly variable densities due to its reliance on a globally fixed neighborhood radius, HDBSCAN can adaptively adjust the neighborhood radius based on local density variations, making it more robust for clustering raw VBSs generated from facades of varying sizes and orientations.

### C. Coverage Computation and Database Storage

After valid VBS locations have been clustered, the remaining task is to determine the coverage entries of the VBS database. To efficiently store this spatial coverage information, the service region is discretized into a  $D_x \times D_y$  grid at the user height slice  $z = h_{UE}$ , as illustrated in Fig. 2(c). The spatial coverage associated with the physical BS and each clustered VBS is characterized by a discrete coordinate set  $\mathcal{C}_v$ . Specifically,  $\mathcal{C}_0$  aggregates the grid points providing direct LoS service, while each  $\mathcal{C}_v$  ( $v \geq 1$ ) encapsulates the VLoS coverage extended by the  $v$ -th VBS link.

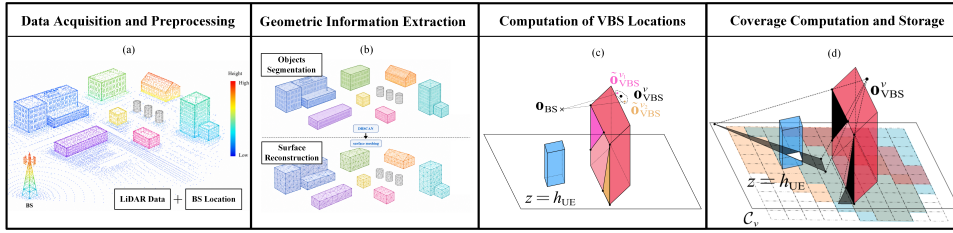


Fig. 2: Workflow of the offline VBS database construction: (a) Input regional 3D LiDAR point cloud and BS location; (b) Segment static buildings and reconstruct irregular triangular meshes; (c) Compute and cluster candidate VBS positions to mitigate noise; (d) Discretize the region into grids to compute and store VLoS coverage areas in a quantized form.

To populate these coverage sets, each grid point  $\mathbf{o}_g = (i_x, i_y, h_{UE})$  on the quantized slice is evaluated by tracing a line segment toward the corresponding source coordinates. For the LoS coverage  $\mathcal{C}_0$ , a grid point  $\mathbf{o}_g$  is included if the segment connecting it to  $\mathbf{o}_{BS}$  is entirely free of environmental occlusions, i.e.,  $\sum_{\forall j} \text{Intersect}(\mathbf{o}_{BS}, \mathbf{o}_g, \mathcal{T}_j) = 0$ . For the VLoS coverage  $\mathcal{C}_v$  ( $v \geq 1$ ), the segment is directed toward the cluster center  $\mathbf{o}_{VBS}^v$ . A grid point  $\mathbf{o}_g$  is included in  $\mathcal{C}_v$  if and only if the segment intersects a designated reflector triangle  $\mathcal{T}_i$  associated with that cluster, while remaining unobstructed by any other mesh  $\mathcal{T}_j$  ( $j \neq i$ ) along both the incident and reflected sub-segments, as depicted in Fig. 2(d).

Finally, the completed VBS database centralizes and stores these decoupled geometric entries as  $\{\mathbf{o}_{BS}, \mathcal{C}_0\}$  and  $\{\mathbf{o}_{VBS}^v, \mathcal{C}_v\}_{v \geq 1}$  on the quantized grid. Compared with measurement-intensive CKM-based methods that rely on dense high-dimensional channel parameter tables [28], the proposed database structure provides a highly compact, storage-efficient alternative that remains structurally consistent with the dominant-path assumption in high-frequency propagation. Once constructed, this lightweight database alone is sufficient to support subsequent beam management, allowing the high-dimensional raw LiDAR data to be permanently discarded from the online system.

#### IV. VBS-GUIDED MU-MIMO BEAM MANAGEMENT

In this section, we present the VBS-guided MU-MIMO beam management framework by developing the VBS-assisted coarse channel reconstruction, VOP-based partial beam training, and DD3QN-CBS algorithm. At the framework level, the offline VBS database described in Section III is converted into a VBS-assisted coarse beamspace representation, which is subsequently calibrated through online partial beam training for interference-aware multi-user coordination.

As illustrated in Fig. 3, the proposed framework consists of three sequential stages. First, the spatial relations among the BS, VBSs, and users are mapped into the channel domain, producing a coarse beamspace representation. Second, since this representation is derived from the VBS database and may be affected by LiDAR noise, reconstruction errors, and grid quantization, a VOP-based partial beam training scheme is designed to measure and refine the most promising candidate beam entries with limited online overhead. Finally, the refined online measurements and the VBS-assisted coarse beamspace representation are jointly incorporated into the DD3QN-CBS algorithm to perform coordinated MU-MIMO beam selection under multi-user interference. The details of these three stages are presented as follows.

##### A. VBS-assisted Coarse Channel Reconstruction

This subsection details the transformation of the offline VBS database into the coarse channel estimates. By extracting path parameters, such as angle-of-arrival (AoA) and angle-of-departure (AoD), from the stored locations and coverage regions, the system constructs this representation to guide subsequent beam training and selection.

###### 1) Possible AoA and AoD Computation

Given the user location and the VBS database, the BS first identifies the available LoS or VLoS paths through  $\mathcal{C}_0$  and  $\{\mathcal{C}_v\}_{v \geq 1}$ . To map these active propagation paths into precise angular coordinates, the system calculates the physical reflection point for each active VLoS path. Specifically, for a clustered VBS  $v \geq 1$ , let  $\mathbf{p}_{BS}^v = \mathbf{o}_{ref}^v - \mathbf{o}_{BS}$  and  $\mathbf{p}_{UE}^v = \mathbf{o}_{ref}^v - \mathbf{o}_{UE}$  denote the displacement vectors from the reflection point associated with VBS  $v$  to the BS and the user, respectively. The coordinates of the reflection point  $\mathbf{o}_{ref}^v$  can be computed from the VBS center  $\mathbf{o}_{VBS}^v$  via geometric mirror relations as

$$\mathbf{o}_{ref}^v = \mathbf{o}_{VBS}^v + \frac{\|\mathbf{o}_{BS} - \mathbf{o}_{VBS}^v\|_2^2 (\mathbf{o}_{UE} - \mathbf{o}_{VBS}^v)}{2 (\mathbf{o}_{BS} - \mathbf{o}_{VBS}^v)^T (\mathbf{o}_{UE} - \mathbf{o}_{VBS}^v)}. \quad (11)$$

For the LoS path, when it is present, the corresponding displacement vectors are  $\mathbf{p}_{BS}^0 = \mathbf{o}_{UE} - \mathbf{o}_{BS}$  and  $\mathbf{p}_{UE}^0 = \mathbf{o}_{BS} - \mathbf{o}_{UE}$ . We introduce a unified geometric mapping  $f[\cdot; \cdot, \cdot]$  defined as

$$f[\mathbf{p}; \Delta\phi, \Delta\psi] \triangleq \begin{bmatrix} \arctan\left(\frac{\{\mathbf{p}\}_2}{\{\mathbf{p}\}_1}\right) + \Delta\phi \\ \arccos\left(\frac{\{\mathbf{p}\}_3}{\|\mathbf{p}\|_2}\right) + \Delta\psi \end{bmatrix}, \quad (12)$$

where the array azimuth and elevation offsets at the user and BS are denoted as  $\Delta\phi^r, \Delta\phi^t$  and  $\Delta\psi^r, \Delta\psi^t$ , respectively. Using (12), the user-side and BS-side geometric parameters for both VLoS paths and the LoS path are obtained as  $[\hat{\phi}_v^r, \hat{\psi}_v^r, \hat{r}_v^r]^T = f[\mathbf{p}_{UE}^v; \Delta\phi^r, \Delta\psi^r]$ ,  $[\hat{\phi}_v^t, \hat{\psi}_v^t, \hat{r}_v^t]^T = f[\mathbf{p}_{BS}^v; \Delta\phi^t, \Delta\psi^t]$ ,  $[\hat{\phi}_0^r, \hat{\psi}_0^r, \hat{r}_0^r]^T = f[\mathbf{p}_{UE}^0; \Delta\phi^r, \Delta\psi^r]$ , and  $[\hat{\phi}_0^t, \hat{\psi}_0^t, \hat{r}_0^t]^T = f[\mathbf{p}_{BS}^0; \Delta\phi^t, \Delta\psi^t]$ , where  $\hat{\phi}_v^r$  and  $\hat{\psi}_v^r$  represent the estimated user-side azimuth and elevation angles for path  $v$ , respectively, while  $\hat{\phi}_v^t$  and  $\hat{\psi}_v^t$  represent the corresponding BS-side angles. The distances from the reflection point to the user and BS are denoted by  $\hat{r}_v^r$  and  $\hat{r}_v^t$ , respectively, while  $\hat{r}_0^r = \hat{r}_0^t$  represents the LoS distance between the user and BS.

These geometric quantities determine the plausible departure and arrival directions. With the path geometry fixed, the next step is to assign each candidate path a reasonable path gain before synthesizing an initial channel estimate.

## 2) Path Loss Computation

Since the VBS database is derived from environmental geometry, it does not contain reliable material properties required for accurate reflection modeling, such as reflection coefficients or surface-dependent attenuation factors. Accordingly, the path loss is modeled using free-space propagation with an additional reflection loss for VLoS paths. This simplified model is adopted because the coarse channel reconstruction is intended to rank candidate beams and narrow the search space, rather than to substitute for high-fidelity electromagnetic simulations. Let  $d_0 = \|\mathbf{p}_{\text{BS}}^0\|_2$  and  $d_v = \|\mathbf{p}_{\text{UE}}^v\|_2 + \|\mathbf{p}_{\text{BS}}^v\|_2$ . The LoS ( $v = 0$ ) and VLoS path ( $v \geq 1$ ) losses are directly expressed as

$$\begin{aligned} \text{PL}_0 &= 20 \log_{10} \left( \frac{4\pi f_c}{c} \right) + 20 \log_{10}(d_0), \\ \text{PL}_v &= 20 \log_{10} \left( \frac{4\pi f_c}{c} \right) + 20 \log_{10}(d_v) + \Gamma, \end{aligned} \quad (13)$$

where  $f_c$  is the carrier frequency,  $c$  is the speed of light, and  $\Gamma$  is a predefined effective reflection loss term that models unknown material attenuation. With  $\text{PL}_v$  defined for both LoS and VLoS paths, the corresponding complex path amplitude is uniformly approximated as  $\hat{\beta}_v = 10^{-\frac{\text{PL}_v}{20}}$ .

## 3) Coarse Channel Reconstruction

Building upon the geometric information derived in the previous subsections, this stage synthesizes a coarse channel matrix to identify the dominant spatial directions. Due to point-cloud measurement noise and quantization errors in the stored coverage regions, relying on a single nearest grid point may omit useful propagation paths. To make the retrieval process less sensitive to such errors, we relax the search criteria by mapping the user location to two K-nearest-neighbor (KNN) grid-index sets, including  $\mathcal{K}_0$  for the direct LoS path and  $\mathcal{K}_v$  for the reflected VLoS paths. In practice, these two neighborhoods can have different sizes to reflect the different uncertainty levels of direct and reflected coverage. The candidate path set  $\mathcal{V}_{\text{UE}}$  is then formed as

$$\mathcal{V}_{\text{UE}} = \{v \mid \mathcal{C}_v \cap \mathcal{K}_v \neq \emptyset, v \geq 0\}. \quad (14)$$

Given  $\mathcal{V}_{\text{UE}}$ , we reconstruct the coarse channel  $\hat{\mathbf{H}}$  by aggregating all identified paths through a unified summation, which can be expressed as

$$\hat{\mathbf{H}} = \sqrt{N_{\text{BS}} N_{\text{UE}}} \sum_{v \in \mathcal{V}_{\text{UE}}} \hat{\beta}_v e^{j\Xi_v} \mathbf{a}(\hat{\nu}_v; N_{\text{UE}}) \mathbf{a}(\hat{\mu}_v; N_{\text{BS}})^H, \quad (15)$$

where the array response vector  $\mathbf{a}(\cdot; \cdot)$  follows the definition in (5), and the estimated BS-side and user-side spatial frequencies for path  $v$  are defined as functions of the physical geometric angles, i.e.,  $\hat{\mu}_v = \cos(\hat{\phi}_v^t) \sin(\hat{\psi}_v^t)$  and  $\hat{\nu}_v = \cos(\hat{\phi}_v^r) \sin(\hat{\psi}_v^r)$ . For the LoS path term, the phase is deterministic and set as  $\Xi_0 = -\frac{2\pi f_c}{c} \|\mathbf{p}_{\text{BS}}^0\|_2$ , where  $f_c$  is the carrier frequency and  $c$  is the speed of light. For reflected paths,  $\Xi_v \sim \mathcal{U}(0, 2\pi)$  denotes independent random phases reflecting the uncorrelated scattering assumption in [19]. By preserving these core spatial signatures,  $\hat{\mathbf{H}}$  provides a coarse channel representation for ranking beam pairs and narrowing the search space in the subsequent partial training phase.

## B. VOP-based Partial Beam Training

The VBS-assisted coarse channel reconstruction in the previous subsection provides an initial channel estimate for each user based on the available LoS and VLoS geometric paths. However, this estimate may deviate from the actual wireless channel due to LiDAR noise, grid quantization, unknown reflection properties, and unmodeled scattering components. To refine the coarse estimate without considerable beam sweeping overhead, this subsection develops a VOP-based partial beam training scheme, where the reconstructed coarse channels are projected onto the BS-side and user-side beam codebooks to identify beam pairs that are likely to contain dominant channel energy. Online pilot training is then performed only over these promising directions, so the coarse reconstruction provides the measurement plan while the pilot responses provide channel-aware calibration.

A key design issue is that online calibration and final coordinated beam selection require different levels of pruning. The measured beam set should be small to control training overhead, whereas the feasible set for final beam selection should remain broader to retain optimal joint beam configurations. Therefore, we adopt a two-level beam subset design: the search subsets specify the beam indices measured online, while the candidate subsets define the feasible beam indices for later beam selection.

### 1) Beam Search and Candidate Subset Construction

This stage constructs the two-level beam subsets by first mapping the reconstructed coarse channel estimates into the codebook beam domain. For the  $k$ -th user, the coarse channel estimate  $\hat{\mathbf{H}}_k$  is projected onto the BS-side and user-side DFT codebooks, yielding the coarse beamspace gain matrix  $\hat{\mathbf{G}}_k = \mathbf{U}_{\text{UE}}^H \hat{\mathbf{H}}_k \mathbf{U}_{\text{BS}}$ . The BS-side and user-side DFT codebook matrices  $\mathbf{U}_{\text{BS}}$  and  $\mathbf{U}_{\text{UE}}$  are obtained by stacking the codebook vectors in  $\mathcal{F}_{\text{BS}}$  and  $\mathcal{W}_{\text{UE}}$  defined in Section II-A, respectively. They are defined as

$$\begin{aligned} \mathbf{U}_{\text{BS}} &\triangleq \left[ \mathbf{a} \left( \frac{1 - N_{\text{BS}}}{N_{\text{BS}}}; N_{\text{BS}} \right), \dots, \mathbf{a} \left( \frac{N_{\text{BS}} - 1}{N_{\text{BS}}}; N_{\text{BS}} \right) \right], \\ \mathbf{U}_{\text{UE}} &\triangleq \left[ \mathbf{a} \left( \frac{1 - N_{\text{UE}}}{N_{\text{UE}}}; N_{\text{UE}} \right), \dots, \mathbf{a} \left( \frac{N_{\text{UE}} - 1}{N_{\text{UE}}}; N_{\text{UE}} \right) \right]. \end{aligned} \quad (16)$$

Each entry  $\{\hat{\mathbf{G}}_k\}_{i,j}$  represents the coarse predicted gain of the beam pair formed by the  $i$ -th BS-side codeword and the  $j$ -th user-side codeword for user  $k$ . Therefore, subset construction is based on the magnitude ordering of the entries in  $\{\hat{\mathbf{G}}_k\}_{k=1}^K$ . The goal is to form ordered BS-side and user-side beam lists from which both the candidate subsets and the search subsets can be extracted.

Algorithm 1 implements this ordering through a greedy selection procedure. At each iteration, the triplet  $(k, i, j)$  with the largest  $|\{\hat{\mathbf{G}}_k\}_{i,j}|$  is selected, where  $i$  and  $j$  denote the BS-side and user-side beam indices, respectively. If the selected BS-side index has not been included and the target BS candidate size has not been reached, it is appended to the ordered BS-side list. Similarly, the selected user-side index is appended to the ordered list of user  $k$  when it is new and the target user candidate size has not been reached. The selected entry is then removed from further consideration,

---

**Algorithm 1** Beam Search and Candidate Subset Construction
 

---

- 1: **Input:** Coarse beamspace  $\{\hat{\mathbf{G}}_k\}_{k=1}^K$ , target sizes  $\tilde{N}_{\text{BS}}, \tilde{N}_{\text{UE}}, \tilde{N}_{\text{BS}}, \tilde{N}_{\text{UE}}$ .
  - 2: **Output:**  $\mathcal{I}_{\text{BS}}, \mathcal{I}_{\text{UE}}^k$  and  $\tilde{\mathcal{I}}_{\text{BS}}, \tilde{\mathcal{I}}_{\text{UE}}^k$ .
  - 3: Initialize ordered lists  $\mathcal{I}_{\text{BS}} = \emptyset, \mathcal{I}_{\text{UE}}^k = \emptyset, \forall k$ .
  - 4: Create copies  $\hat{\mathbf{G}}_k^{\text{copy}} = \hat{\mathbf{G}}_k$ .
  - 5: **while**  $|\mathcal{I}_{\text{BS}}| < \tilde{N}_{\text{BS}}$  or  $\exists k : |\mathcal{I}_{\text{UE}}^k| < \tilde{N}_{\text{UE}}$  **do**
  - 6:   Find  $(k_s, i, j) = \arg \max_{k,i,j} \{|\hat{\mathbf{G}}_k^{\text{copy}}\}_{i,j}$ .
  - 7:   **if**  $i \notin \mathcal{I}_{\text{BS}}$  and  $|\mathcal{I}_{\text{BS}}| < \tilde{N}_{\text{BS}}$  **then**
  - 8:     Append  $i$  to  $\mathcal{I}_{\text{BS}}$ .
  - 9:   **end if**
  - 10:   **if**  $j \notin \mathcal{I}_{\text{UE}}^{k_s}$  and  $|\mathcal{I}_{\text{UE}}^{k_s}| < \tilde{N}_{\text{UE}}$  **then**
  - 11:     Append  $j$  to  $\mathcal{I}_{\text{UE}}^{k_s}$ .
  - 12:   **end if**
  - 13:   Set  $\{\hat{\mathbf{G}}_{k_s}^{\text{copy}}\}_{i,j} = -\infty$ .
  - 14: **end while**
  - 15: Select the first  $\tilde{N}_{\text{BS}}$  entries of  $\mathcal{I}_{\text{BS}}$  to form  $\tilde{\mathcal{I}}_{\text{BS}}$ , and select the first  $\tilde{N}_{\text{UE}}$  entries of each  $\mathcal{I}_{\text{UE}}^k$  to form  $\tilde{\mathcal{I}}_{\text{UE}}^k$ .
- 

and the process continues until the required candidate sizes are reached.

After the ordered lists are obtained, the two-level subsets are generated by taking different prefixes of the same lists. The longer prefixes form the candidate subsets  $\mathcal{I}_{\text{BS}}$  and  $\mathcal{I}_{\text{UE}}^k$ , with sizes  $\tilde{N}_{\text{BS}}$  and  $\tilde{N}_{\text{UE}}$ , which define the feasible beam indices for later beam selection. The shorter prefixes form the search subsets  $\tilde{\mathcal{I}}_{\text{BS}}$  and  $\tilde{\mathcal{I}}_{\text{UE}}^k$ , with sizes  $\tilde{N}_{\text{BS}}$  and  $\tilde{N}_{\text{UE}}$ , which are measured during VOP-based partial beam training.

### 2) Partial Beam Measurements and Feature Synthesis

After the beam search subsets have been selected, the remaining task is to measure these indexed entries rather than the full beamspace grid. This refinement is still nontrivial if users are trained sequentially, since the overhead over the reduced subsets would also scale as  $\lceil \tilde{N}_{\text{BS}}/N_{\text{RF}} \rceil \tilde{N}_{\text{UE}} K$ , where  $\lceil \cdot \rceil$  denotes the ceiling function. The proposed VOP-based scheme addresses this issue by combining VBS-guided subset construction with OP-based concurrent pilot transmission. The former reduces the measured BS-side and user-side beam dimensions from  $N_{\text{BS}}$  and  $N_{\text{UE}}$  to  $\tilde{N}_{\text{BS}}$  and  $\tilde{N}_{\text{UE}}$ , while the latter removes the user-wise sequential factor by allowing all users to transmit distinguishable pilots simultaneously. Exhaustive sequential training has overhead  $\lceil N_{\text{BS}}/N_{\text{RF}} \rceil N_{\text{UE}} K$  [5], and blind OP-based training over the full codebooks still requires  $\lceil N_{\text{BS}}/N_{\text{RF}} \rceil N_{\text{UE}}$  slots [29]. In contrast, the proposed scheme requires  $\lceil \tilde{N}_{\text{BS}}/N_{\text{RF}} \rceil \tilde{N}_{\text{UE}}$  training slots.

For compact notation, let  $\bar{\mathbf{b}} = [\bar{b}_1, \dots, \bar{b}_{\tilde{N}_{\text{BS}}}]$  denote the ordered BS-side indices in  $\tilde{\mathcal{I}}_{\text{BS}}$ , and let  $\bar{\mathbf{u}}^k = [\bar{u}_1^k, \dots, \bar{u}_{\tilde{N}_{\text{UE}}}^k]$  denote the ordered user-side indices in  $\tilde{\mathcal{I}}_{\text{UE}}^k$ . The  $m$ -th BS training group is defined as

$$\mathcal{B}_m = \{\bar{b}_\ell \mid \ell = (m-1)N_{\text{RF}} + 1, \dots, mN_{\text{RF}}\}, \quad (18)$$

with the last group truncated if necessary. Specifically, we adopt an uplink pilot training procedure. In each training slot  $(m, n)$ , all  $K$  users concurrently transmit their pilot symbols using their respective combiner columns

$$\mathbf{w}_k^{(n)} = \{\mathbf{U}_{\text{UE}}\}_{:, \bar{u}_n^k}. \quad (19)$$

The BS receives the overlapped signals using the analog combiner

$$\mathbf{F}_{\text{RF}}^{(m)} = \{\mathbf{U}_{\text{BS}}\}_{:, \mathcal{B}_m}. \quad (20)$$

Orthogonal pilots  $\boldsymbol{\phi}_k \in \mathbb{C}^{1 \times \tau}$  are employed to differentiate the uplink pilot signals from different users at the BS, satisfying  $\boldsymbol{\phi}_k \boldsymbol{\phi}_j^H = 1$  if  $k = j$  and 0 otherwise, where  $\tau \geq K$  is the pilot length. Under this setup, the received signal matrix  $\mathbf{Y}^{(m,n)} \in \mathbb{C}^{N_{\text{RF}} \times \tau}$  is expressed as [29]

$$\mathbf{Y}^{(m,n)} = \sum_{k=1}^K \sqrt{\tau P_p} (\mathbf{F}_{\text{RF}}^{(m)})^H \mathbf{H}_k^T \mathbf{w}_k^{(n)} \boldsymbol{\phi}_k + (\mathbf{F}_{\text{RF}}^{(m)})^H \mathbf{N}, \quad (21)$$

where  $P_p$  is the pilot transmit power and  $\mathbf{N}$  is the additive white Gaussian noise with entries following  $\mathcal{CN}(0, N_0 W)$ . By correlating the received signal with the corresponding pilot  $\boldsymbol{\phi}_k$ , the BS leverages this orthogonality to suppress inter-user interference and decode the measurement vector  $\mathbf{g}_k^{(m,n)} \in \mathbb{C}^{N_{\text{RF}} \times 1}$  for the  $k$ -th user, which can be expressed as

$$\begin{aligned} \mathbf{g}_k^{(m,n)} &= \frac{1}{\sqrt{\tau P_p}} \mathbf{Y}^{(m,n)} \boldsymbol{\phi}_k^H \\ &= (\mathbf{F}_{\text{RF}}^{(m)})^H \mathbf{H}_k^T \mathbf{w}_k^{(n)} + \frac{1}{\sqrt{\tau P_p}} (\mathbf{F}_{\text{RF}}^{(m)})^H \mathbf{N} \boldsymbol{\phi}_k^H. \end{aligned} \quad (22)$$

After completing the measurements across all training slots, the decoded vectors  $\mathbf{g}_k^{(m,n)}$  are assigned to populate a measured beamspace matrix  $\tilde{\mathbf{G}}_k \in \mathbb{C}^{\tilde{N}_{\text{UE}} \times \tilde{N}_{\text{BS}}}$ , which is initialized to zero. The entries are filled according to the measured indices, such that the  $(i, j)$ -th entry of  $\tilde{\mathbf{G}}_k$  corresponding to the measured BS and user beams is assigned the value of  $\mathbf{g}_k^{(m,n)}$ . Formally, this mapping can be expressed as

$$\{\tilde{\mathbf{G}}_k\}_{\bar{u}_n^k, \mathcal{B}_m} = (\mathbf{g}_k^{(m,n)})^T. \quad (23)$$

Finally, we extract the effective beamspace submatrices corresponding to the candidate subsets  $\tilde{\mathcal{I}}_{\text{BS}}$  and  $\tilde{\mathcal{I}}_{\text{UE}}^k$  to obtain a compact beamspace feature representation. We denote the online beamspace feature and the coarse beamspace feature as

$$\mathbf{X}_k^{\text{meas}} = \{\tilde{\mathbf{G}}_k\}_{\tilde{\mathcal{I}}_{\text{UE}}^k, \tilde{\mathcal{I}}_{\text{BS}}}, \quad \mathbf{X}_k^{\text{coar}} = \{\hat{\mathbf{G}}_k\}_{\tilde{\mathcal{I}}_{\text{UE}}^k, \tilde{\mathcal{I}}_{\text{BS}}}. \quad (24)$$

These two features are concatenated to form a beamspace feature set that combines the VBS-assisted coarse beamspace representation with the calibrated online measurements.

### C. VBS-guided DD3QN-CBS

This subsection explains how the coarse beamspace features and refined online measurements are used to make the final beam decisions through the proposed VBS-guided DD3QN-CBS algorithm. After candidate pruning, the task is reduced from full-codebook search to selecting a joint beam configuration from the candidate spaces. This reduced problem is still nontrivial because the beam choices of different users are coupled through inter-user interference, and the ESE objective in (4a) is available only after the BS beams, user beams, and digital precoder are jointly determined.

Direct exhaustive search is still expensive since the BS must select  $N_{\text{RF}}$  beams from  $\tilde{N}_{\text{BS}}$  candidates and the  $K$  users jointly contribute  $\tilde{N}_{\text{UE}}^K$  user-side choices, leading to  $\frac{\tilde{N}_{\text{BS}}! \tilde{N}_{\text{UE}}^K}{N_{\text{RF}}! (N_{\text{BS}} - N_{\text{RF}})!}$  feasible configurations [29]. This objective

motivates a sequential decision view of the original joint beam selection problem: the system can incrementally construct one joint configuration by selecting beams step by step.

Hence, we reformulate coordinated beam selection over the candidate subsets as a finite-horizon leader-follower Markov game [30]. This reformulation does not change the original ESE maximization objective in (4a). Instead, it provides a tractable decision model for constructing the joint beam selection solution sequentially. In each episode, the system constructs one joint configuration step by step. In this paper, we adopt the common assumption that the number of simultaneously served users equals the number of RF chains, i.e.,  $K = N_{\text{RF}}$ . The BS-side agent first selects a transmit beam because BS beams are shared across users and shape the effective multi-user channel, and the user-side agent then selects the receive beam conditioned on the previous BS-side decisions.

Under this formulation, the state records both the beamspace features and the beam decisions already made. Since these selected beams are explicitly embedded into the state, the next state and immediate rewards depend only on the current state and the current actions  $(p_t, q_t)$ , making the sequential construction compatible with the Markov property. To further improve learning efficiency, we introduce BS-side action masking to avoid invalid reuse of already selected transmit beams and design dense intermediate rewards to alleviate the sparse terminal-reward issue. The overall framework is illustrated in Fig. 3(c).

The resulting Markov game is formulated as

$$\mathcal{M} = \langle \mathcal{S}, \mathcal{A}_{\text{BS}}, \mathcal{A}_{\text{UE}}, \mathcal{P}, \mathcal{R}_{\text{BS}}, \mathcal{R}_{\text{UE}}, \gamma \rangle, \quad (25)$$

where  $\mathcal{S}$  is the state space,  $\mathcal{A}_{\text{BS}}$  and  $\mathcal{A}_{\text{UE}}$  are the action spaces for the BS-side and user-side agents, respectively,  $\mathcal{R}_{\text{BS}}$  and  $\mathcal{R}_{\text{UE}}$  are the reward functions for the BS-side and user-side agents, and  $\gamma$  is the discount factor. The transition kernel is defined as  $s_{t+1} \sim \mathcal{P}(\cdot | s_t, p_t, q_t)$ . We index the decision step as  $t = 0, \dots, K-1$ , while the physical user index is  $k = 1, \dots, K$ , thus step  $t$  corresponds to the  $(t+1)$ -th scheduled user. The BS-side policy  $\pi_{\text{BS}}$  first selects a relative transmit-beam index  $p_t$  according to  $\pi_{\text{BS}}(p_t | s_t)$ . Conditioned on this leader action, the user-side policy  $\pi_{\text{UE}}$  selects a relative receive-beam index  $q_t$  according to  $\pi_{\text{UE}}(q_t | \tilde{s}_t)$ , where  $\tilde{s}_t \triangleq (s_t, p_t)$  augments the state with the BS-side action [30]. The corresponding physical codeword indices are obtained from the candidate subsets as  $\tilde{p}_t \triangleq \{\mathcal{I}_{\text{BS}}\}_{p_t}$  and  $\tilde{q}_t \triangleq \{\mathcal{I}_{\text{UE}}^{t+1}\}_{q_t}$ . This hierarchy keeps the BS-side decision visible to the user-side policy and therefore matches the interference-coupled nature of MU-MIMO beam selection.

Each agent  $i \in \{\text{BS}, \text{UE}\}$  receives an instantaneous reward  $r_t^i$ . Although the intermediate rewards are different, the two agents are cooperative because they share the same terminal objective, namely maximizing the ESE in (4a). The policy pair  $\pi = (\pi_{\text{BS}}, \pi_{\text{UE}})$  is therefore trained to maximize the expected discounted return

$$J_i = \mathbb{E}_{\pi, \mathcal{P}} \left[ \sum_{\ell=0}^{K-1-t} \gamma^\ell r_{t+\ell}^i \right]. \quad (26)$$

To evaluate this long-term return, each agent learns an action-value Q-function  $Q(\cdot)$ , which quantifies the expected cumula-

tive discounted reward of taking a specific action under state  $s_t$  and subsequently following policy  $\pi$ .

Following the hierarchical information structure, the BS-side agent maintains  $Q_{\text{BS}}(s_t, p_t)$  to evaluate its transmit beam selections. Since the user-side agent observes the leader's action  $p_t$  before executing its own, its decision-making is modeled by the joint action-value function  $Q_{\text{UE}}(s_t, p_t, q_t)$ . These action-value functions satisfy the Bellman optimality equations, which can be expressed as

$$\begin{aligned} Q_{\text{BS}}^*(s_t, p_t) &= \mathbb{E}_{\mathcal{P}} \left[ r_t^{\text{BS}} + \gamma \max_{p_{t+1}} Q_{\text{BS}}^*(s_{t+1}, p_{t+1}) \right], \\ Q_{\text{UE}}^*(s_t, p_t, q_t) &= \mathbb{E}_{\mathcal{P}} \left[ r_t^{\text{UE}} + \gamma \max_{q_{t+1}} Q_{\text{UE}}^*(s_{t+1}, p_{t+1}^*, q_{t+1}) \right], \end{aligned} \quad (27)$$

where  $p_{t+1}^* = \arg \max_p Q_{\text{BS}}^*(s_{t+1}, p)$  represents the predicted optimal action of the leader at the next state, and the expectation is taken over the environment transition kernel  $\mathcal{P}$ .

The above equations define the coupled optimality condition under ideal conditions. However, finding exact analytical solutions for  $Q_{\text{BS}}^*$  and  $Q_{\text{UE}}^*$  is computationally intractable due to the continuous and high-dimensional observation space. To circumvent this challenge, the proposed DD3QN-CBS framework employs dueling double deep-Q-network (D3QN) [31] to parameterize and approximate these optimal Q-functions, denoted as  $Q_{\text{BS}}(s_t, p_t; \Theta_{\text{BS}})$  and  $Q_{\text{UE}}(s_t, p_t, q_t; \Theta_{\text{UE}})$ , where  $\Theta_{\text{BS}}$  and  $\Theta_{\text{UE}}$  represent the parameters of the online networks.

To mitigate the inherent overestimation bias in discrete action spaces, the target values  $y_t^{\text{BS}}$  and  $y_t^{\text{UE}}$  are evaluated using the double Q-network principle by decoupling action selection from evaluation, which can be expressed as

$$\begin{aligned} y_t^{\text{BS}} &= r_t^{\text{BS}} + \gamma Q_{\text{BS}}(s_{t+1}, p_{t+1}^*; \Theta'_{\text{BS}}), \\ y_t^{\text{UE}} &= r_t^{\text{UE}} + \gamma Q_{\text{UE}}(s_{t+1}, p_{t+1}^*, q_{t+1}^*; \Theta'_{\text{UE}}), \end{aligned} \quad (28)$$

where  $\Theta'$  denotes the parameters of the target networks, and  $p_{t+1}^* = \arg \max_p Q_{\text{BS}}(s_{t+1}, p; \Theta_{\text{BS}})$  and  $q_{t+1}^* = \arg \max_q Q_{\text{UE}}(s_{t+1}, p_{t+1}^*, q; \Theta_{\text{UE}})$  are the actions selected by the corresponding online networks. To enhance learning stability and sample efficiency under sparse feedback, both agents adopt a dueling network architecture that decomposes the parameterized action-value function into a state-value stream and an advantage stream as follows

$$\begin{aligned} Q_i(s, a; \Theta_i) &= V_i(s; \Theta_i) + A_i(s, a; \Theta_i) \\ &\quad - \frac{1}{|\mathcal{A}_i|} \sum_{a' \in \mathcal{A}_i} A_i(s, a'; \Theta_i). \end{aligned} \quad (29)$$

The above formulation establishes the mathematical principles governing how the two agents interact and how their parameterized Q-networks are updated. To complete the algorithmic framework, the subsequent sections elaborate on the concrete definitions of the foundational DRL components, i.e., the state space, action space, reward function, and network architecture.

### 1) State Space

The state space is structured to capture both the latent channel quality and the sequential decision history. Specifically, the BS-side and user-side agents share a composite input tensor  $\mathfrak{G}_{\text{in}} \in \mathbb{R}^{4 \times \tilde{N}_{\text{BS}} \times \tilde{N}_{\text{UE}} \times K}$ , constructed by stacking four information channels: action mask  $\mathfrak{A}_t$ , measurement mask  $\mathfrak{M}$ , coarse beamspace features  $\{\mathbf{X}_k^{\text{coar}}\}_{k=1}^K$ , and online beamspace features  $\{\mathbf{X}_k^{\text{meas}}\}_{k=1}^K$ . The action mask is binary, where one

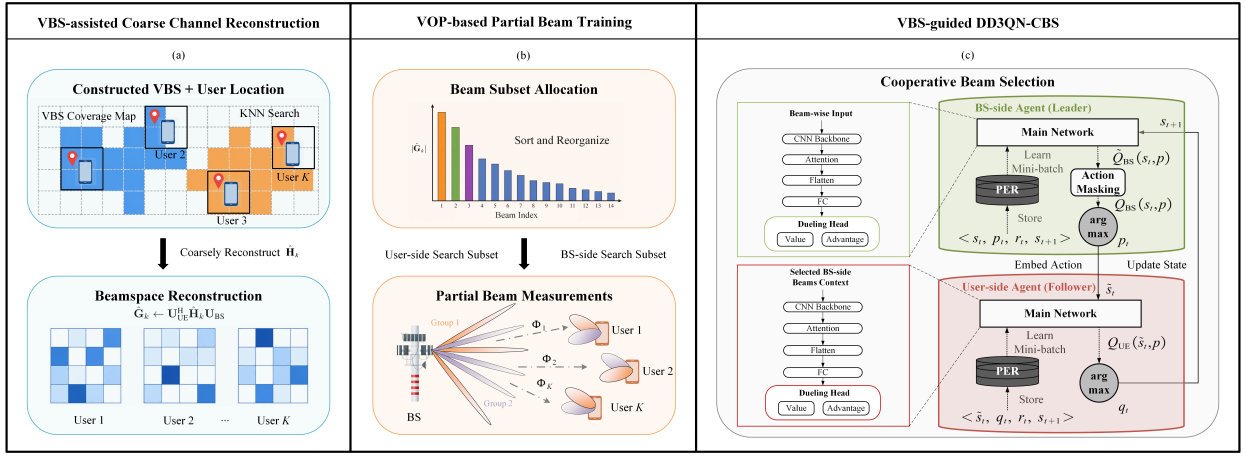


Fig. 3: Proposed VBS-guided MU-MIMO beam management framework. (a) After constructing the VBS database offline, the BS performs coarse channel reconstruction to obtain the VBS-assisted coarse beamspace representation; (b) a VOP-based partial beam training scheme measures the selected candidate beam entries to refine this representation; (c) a dual-agent DD3QN-CBS algorithm is developed for interference-aware beam selection.

indicates an available action and zero indicates a previously selected beam. The measurement mask is also binary, where one indicates that the corresponding beam entry has been measured and zero indicates an unmeasured entry.

The action mask is updated according to the leader-follower order. After the BS-side agent selects beam index  $p_t$ , the corresponding BS-side vector in the current user slice is marked as unavailable, which is expressed as

$$\{\mathcal{A}_t\}_{p_t, :, t+1} = \mathbf{0}_{\tilde{N}_{UE}}. \quad (30)$$

This partially updated state is then passed to the user-side agent as a conditional observation. After the user-side agent selects  $q_t$  for the  $(t+1)$ -th scheduled user, the corresponding user-side vector in the same user slice is also marked as unavailable, which can be written as

$$\{\mathcal{A}_t\}_{:, q_t, t+1} = \mathbf{0}_{\tilde{N}_{BS}}. \quad (31)$$

This ordered state mutation makes the current BS-side choice visible to the user-side agent and records the accumulated BS-side and user-side beam occupancy across the episode. The fixed measurement mask separately records which beamspace entries have been calibrated by VOP-based beam training.

## 2) Action Space

To limit strong multi-user interference, the action space should be constrained against highly correlated beam assignments that cause equivalent channel rank degradation [8], [29]. Specifically, if multiple concurrent users are assigned to the identical BS codeword, the resulting effective channel matrix will contain identical columns, rendering it structurally low-rank. Consequently, the composite channel-precoder matrix cannot be diagonalized regardless of the digital precoder design  $\mathbf{F}_{BB}$  at the BS-side, thereby weakening spatial multiplexing capability and reducing the ESE.

Instead of penalty-based collision avoidance [8], we employ action masking during decision making [32], [33]. This maintains a consistent network architecture and accelerates training by allowing agents to focus exclusively on ranking the relative quality of valid beam pairs.

Following the same leader-follower order, the BS-side feasible action set is defined first. Starting from  $\mathcal{A}_{BS}^0 = \{1, \dots, \tilde{N}_{BS}\}$ , the feasible set is updated recursively by re-

moving the relative beam index  $p_{t-1}$  selected in the previous step, which is expressed as

$$\mathcal{A}_{BS}^t = \mathcal{A}_{BS}^{t-1} \setminus \{p_{t-1}\}, \quad t = 1, \dots, K-1. \quad (32)$$

The masking process is implemented by forcing the Q-values of these previously selected BS-side beams to  $-\infty$ . Consequently, while the output dimension of the BS-side network remains fixed at  $|\mathcal{A}_{BS}^0|$ , its masked Q-value function is defined as

$$\tilde{Q}_{BS}(s_t, p) = \begin{cases} Q_{BS}(s_t, p), & p \in \mathcal{A}_{BS}^t \\ -\infty, & \text{otherwise} \end{cases}. \quad (33)$$

After the BS-side action is fixed, the user-side action space  $\mathcal{A}_{UE}^t$  represents the relative beam indices within the candidate subset of the currently scheduled user. Although the user-side network has a fixed discrete output dimension  $\tilde{N}_{UE}$ , the decision at step  $t$  is executed only for that specific user. This parameter-sharing design can be viewed as  $K$  homogeneous user agents sharing a single Q-network, which improves sample efficiency and generalization without changing the underlying MU-MIMO coupling.

For exploitation, the BS-side and user-side actions are selected sequentially according to

$$p_t = \arg \max_{p \in \mathcal{A}_{BS}^t} \tilde{Q}_{BS}(s_t, p), \quad (34)$$

$$q_t = \arg \max_{q \in \mathcal{A}_{UE}^t} Q_{UE}(\tilde{s}_t, q). \quad (35)$$

During training, an  $\epsilon$ -greedy exploration strategy is adopted, where each agent randomly samples from its feasible action set with probability  $\epsilon$  and follows the greedy action above with probability  $1 - \epsilon$ . The resulting joint action at time step  $t$  is denoted as  $(p_t, q_t)$ . To further enhance sample efficiency, we employ the prioritized experience replay (PER) buffer [34].

Once the feasible action space is defined, the next challenge is to provide informative training signals before the final ESE becomes available.

## 3) Reward Function

The reward design follows the same principle: the terminal objective should remain the ESE, but the learning signal should not be delayed until the end of the episode. Otherwise, the learning process would lead to inefficient credit assign-

ment and slow convergence. Therefore, the BS-side and user-side rewards are defined in the same decision order using the estimated SINR proxies, while the terminal feedback remains the actual ESE.

Following the leader-follower decision structure, the BS-side immediate reward design should evaluate whether the current transmit beam provides useful multi-user coverage while avoiding overlap with previously selected BS beams. For notation clarity, let  $\mathcal{B}_{<t} \triangleq \{\tilde{p}_i\}_{i=0}^{t-1}$  denote the set of BS beams selected before step  $t$ , with  $\mathcal{B}_{<0} = \emptyset$ . Here,  $\mathbf{G}_k$  denotes the actual beamspace for the  $k$ -th user, and the true beamspace is required only during training. The corresponding utility function is defined as

$$U_t^{\text{BS}}(p_t) = \sum_{k=1}^K \frac{P_T \max_{\tilde{q} \in \mathcal{I}_{\text{UE}}^k} |\{\mathbf{G}_k\}_{\tilde{q}, \tilde{p}_t}|^2}{P_T \sum_{\tilde{p} \in \mathcal{B}_{<t}} \max_{\tilde{q} \in \mathcal{I}_{\text{UE}}^k} |\{\mathbf{G}_k\}_{\tilde{q}, \tilde{p}}|^2 + N_0 W}. \quad (36)$$

The user-side immediate reward is conditioned on the BS-side action and should evaluate the selected receive beam quality while considering SINR. Thus, we also define the user-side utility function as

$$U_t^{\text{UE}}(p_t, q_t) = \frac{P_T |\{\mathbf{G}_{t+1}\}_{\tilde{q}_t, \tilde{p}_t}|^2}{P_T \sum_{\tilde{p} \in \mathcal{B}_{<t}} |\{\mathbf{G}_{t+1}\}_{\tilde{q}_t, \tilde{p}}|^2 + N_0 W}. \quad (37)$$

The resulting reward functions are formulated as

$$r_t^{\text{BS}} = \begin{cases} \alpha_{\text{BS}} g[U_t^{\text{BS}}(p_t)], & t < K - 1, \\ \text{ESE}, & t = K - 1, \end{cases} \quad (38)$$

$$r_t^{\text{UE}} = \begin{cases} \alpha_{\text{UE}} g[U_t^{\text{UE}}(p_t, q_t)], & t < K - 1, \\ \text{ESE}, & t = K - 1, \end{cases} \quad (39)$$

where  $g[\cdot]$  is a normalization function that scales the reward to  $[0, 1]$ , and  $\alpha_{\text{BS}}, \alpha_{\text{UE}}$  are scaling factors.

Upon completing the sequential decisions, the selected BS beam set  $\mathcal{B}_{<K} \subset \mathcal{I}_{\text{BS}}$  and the mapped user-side beam indices determine the analog beamforming matrices. Specifically, the selected DFT submatrices for the analog precoder at the BS and the analog combiner for the  $k$ -th user are represented as  $\mathbf{F}_{\text{RF}} = \{\mathbf{U}_{\text{BS}}\}_{:, \mathcal{B}_{<K}}$  and  $\mathbf{w}_k = \{\mathbf{U}_{\text{UE}}\}_{:, \tilde{q}_{k-1}}$  for  $k = 1, \dots, K$ , respectively. Consequently, the effective channel vector of the  $k$ -th user is determined by  $\mathbf{h}_{\text{eff}}^k = \mathbf{w}_k^H \mathbf{H}_k \mathbf{F}_{\text{RF}} \in \mathbb{C}^{1 \times N_{\text{RF}}}$ . By stacking these individual vectors, the composite effective channel matrix after analog beam selection is formed as  $\mathbf{H}_{\text{eff}} = [\mathbf{h}_{\text{eff}}^1; \dots; \mathbf{h}_{\text{eff}}^K] \in \mathbb{C}^{K \times N_{\text{RF}}}$ .

Utilizing this low-dimensional effective channel matrix  $\mathbf{H}_{\text{eff}}$ , the system performs baseband digital precoding. Considering both computational complexity and multi-user interference mitigation, the minimum mean-square error (MMSE) precoder is adopted for digital baseband precoding, which can be obtained by [35]

$$\mathbf{F}_{\text{BB}} = (\mathbf{H}_{\text{eff}}^H \mathbf{H}_{\text{eff}} + \eta \mathbf{I})^{-1} \mathbf{H}_{\text{eff}}^H, \quad (40)$$

where the regularization parameter  $\eta$  is set to  $N_0 W / P_T$  to balance noise enhancement and inter-user interference suppression.

TABLE I: The simulation parameters configuration.

Parameter	Value
Carrier Frequency $f_c$	40 GHz
Bandwidth $W$	100 MHz
BS Position $\mathbf{o}_{\text{BS}}$	[140, 60, 4] m
BS/user antenna size $N_{\text{BS}}, N_{\text{UE}}$	128, 8
Transmit Power $P_T$	40 dBm
Effective Reflection Loss $\Gamma$	10
KNN for $\mathcal{K}_0$ and $\mathcal{K}_v$	6, 3
VBS Grid Number $D_x, D_y$	40, 40
Learning Rate	$10^{-4}$
Discount Factor $\gamma$	0.98
Scaling Factor $\alpha_{\text{BS}}, \alpha_{\text{UE}}$	20, 5
Batch Size	32
Training Episodes for DD3QN-CBS	6000

#### 4) Network Architecture

Finally, we describe the Q-network architecture used to map the structured beamspace observation to the beam selection actions. Both agents adopt a compact convolutional neural network (CNN) design, where a lightweight two-layer CNN first extracts local beamspace patterns, an attention module recalibrates channel-wise responses [36], and a fully connected (FC) projection maps the flattened features to hidden representations.

For the BS-side agent, each candidate BS beam is represented by the slice  $\mathfrak{G}_b \triangleq \{\mathfrak{G}_{\text{in}}\}_{:, b, :, :} \in \mathbb{R}^{4 \times \tilde{N}_{\text{UE}} \times K}$ , where  $b = 1, \dots, \tilde{N}_{\text{BS}}$ . The shared 2D CNN processes this user-beam plane for every BS candidate and converts it into a compact feature vector after flattening and FC projection. Hence, the BS network preserves the candidate-wise structure and produces one hidden representation for each BS action.

For the user-side agent, the action-mask channel records the BS-side beams selected in previous steps and in the current BS-side decision. Based on this mask, the corresponding selected BS-side beams context is constructed from  $\mathfrak{G}_{\text{in}}$  by gathering the BS-beam rows that have already been committed. This context is then reorganized with respect to each candidate user beam, so that each user-side action is associated with an observation over the selected BS-side beams and the user dimension. In this way, the user-side network is conditioned on the accumulated BS-side selection history without introducing an explicit action-embedding module. Each candidate-specific observation is processed by a similar CNN, attention, and FC projection architecture to obtain one hidden representation for each user-side action.

For each agent, the hidden features are decomposed into a scalar value stream  $V(s) \in \mathbb{R}$  and an advantage stream  $A(s, a) \in \mathbb{R}^{M_{\text{act}}}$ , where  $M_{\text{act}} \in \{\tilde{N}_{\text{BS}}, \tilde{N}_{\text{UE}}\}$ . The final action-value function is obtained by combining the value and advantage streams via (29).

## V. SIMULATION RESULTS

### A. Simulation Setup

The simulation setup is designed to verify whether the proposed offline VBS construction and online beam management pipeline remain effective in a realistic urban layout. The simulation framework is built upon a high-fidelity digital twin integrating Blender and Sionna [37]. We reconstruct a realistic urban scenario based on OpenStreetMap (OSM) data, covering an area of approximately  $120\text{m} \times 120\text{m}$  in Mexia, Texas (Latitude:  $31.6802^\circ$ – $31.6823^\circ$ N, Longitude:

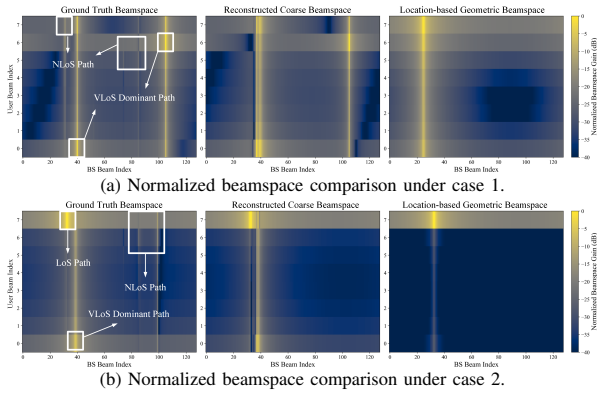


Fig. 4: Visualization of the heatmap of VBS-assisted reconstructed coarse beamspace, pure location-based geometric beamspace, and the ground-truth beamspace.

TABLE II: Averaged NMSE values under different training budgets.

NMSE [dB] \ $\bar{N}_{UE}$	$\bar{N}_{BS}$			
	14	28	42	56
1	-3.87	-4.34	-4.48	-4.54
2	-5.58	-6.76	-7.28	-7.62
3	-6.11	-7.53	-8.37	-8.87

$-96.4826^\circ$ – $-96.4787^\circ$ W). Blender is employed to generate synthetic 3D LiDAR point clouds, while Sionna performs ray-tracing based channel modeling to capture realistic propagation characteristics. To emulate practical sensing imperfections, we introduce Gaussian measurement noise with a standard deviation of 10 cm and a random point drop rate of 10% into the LiDAR data. Users are randomly distributed within unoccupied regions. Detailed system parameters are summarized in Table I.

### B. Performance of Coarse Channel Reconstruction

The coarse channel reconstruction stage is evaluated by comparing the VBS-assisted coarse beamspace representation with the ground-truth beamspace. The performance is quantified by the normalized mean-square error (NMSE) between the normalized true beamspace and the normalized reconstructed beamspace.

The visualization of the normalized beamspace for two cases is shown in Fig. 4. For case 1 shown in Fig. 4(a), the LoS path is blocked, whereas case 2 shown in Fig. 4(b) contains one LoS path and several auxiliary NLoS paths. In both cases, the VBS-assisted coarse beamspace representation captures the dominant spatial directions more effectively than the pure location-based geometric beamspace, which fails to identify the correct beam directions when strong NLoS paths dominate. Although this representation cannot exactly reproduce the true complex channel gain, it provides a reasonable approximation of the relative beam strengths. The averaged NMSE values for these two cases are  $-3.74$  dB and  $-0.18$  dB, respectively, confirming its usefulness for subsequent beam training and selection.

### C. Performance of VOP-based Partial Beam Training

Table II evaluates VOP-based partial beam training for 14 users under the antenna configurations listed in Table I. The reported metric is the NMSE between the true beamspace multi-user channel  $\mathbf{G}_k$  and the measured effective channel  $\tilde{\mathbf{G}}_k$ , which characterizes the reconstruction fidelity under different beam training budgets.

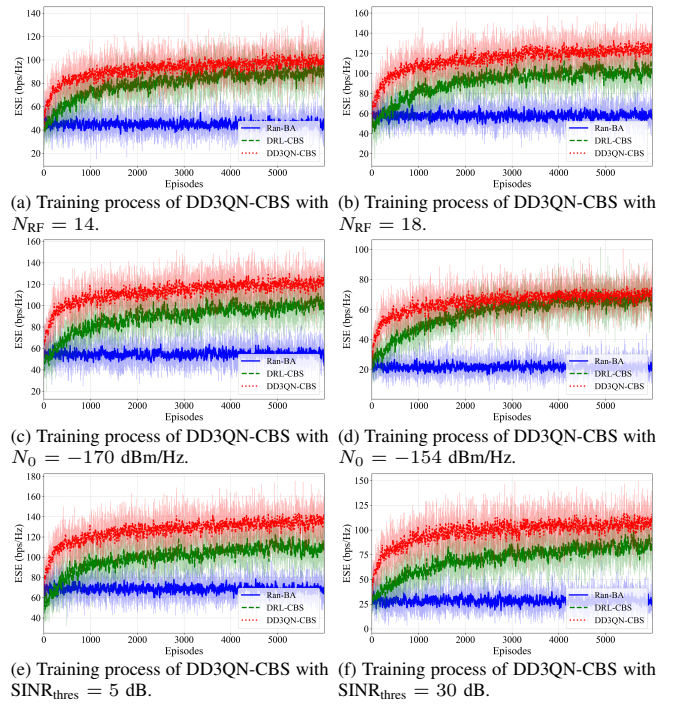


Fig. 5: Training process comparison.

From the results in Table II, the proposed scheme achieves low NMSE with a small training budget, and the reconstruction accuracy improves as the budget increases. Increasing  $\bar{N}_{UE}$  provides a more pronounced improvement than increasing  $\bar{N}_{BS}$ , after which the gains gradually plateau. Consequently, for the subsequent DD3QN-CBS training, we set  $\bar{N}_{BS} = N_{RF}$  and  $\bar{N}_{UE} = 2$  to balance beam training efficiency and beamspace estimation accuracy. These observations highlight the role of VOP-based partial beam training as an online calibration layer that converts the VBS-assisted coarse beamspace representation into reliable beamspace features.

### D. Performance of DD3QN-CBS

DD3QN-CBS is benchmarked against stochastic, heuristic, and learning-based baselines: 1) **Ran-BA** employs a stochastic policy where the BS and users are assigned with beam pairs uniformly at random; 2) **VBS-BA** applies the maximum-magnitude (MM) criterion [38] for beam assignment, entirely based on the VBS-assisted coarse beamspace representation, requiring zero online training; 3) **MM-BA** utilizes the same MM criterion for beam assignment but on a hybrid beamspace, where the coarse beamspace is partially replaced by actual online measurements obtained from VOP-based partial sweeping; 4) **DRL-CBS** serves as a learning-based baseline using the D3QN architecture [8] for beam selection. Since this algorithm was originally designed for single-antenna users with joint precoding, we adapt it by selecting the user-side beam with the largest virtual gain under MMSE precoding. We analyze algorithm behavior across various configurations:  $N_{RF} \in \{14, 16, \dots, 24\}$ ,  $N_0 \in \{-154, -158, \dots, -174\}$  dBm/Hz, and  $\text{SINR}_{\text{thres}} \in \{30, 25, \dots, 5\}$  dB (default:  $N_{RF} = 20$ ,  $N_0 = -174$  dBm/Hz,  $\text{SINR}_{\text{thres}} = 10$  dB).

#### 1) Convergence Performance

As illustrated in Fig. 5, DD3QN-CBS exhibits a faster increase in training ESE than the penalty-based DRL-CBS

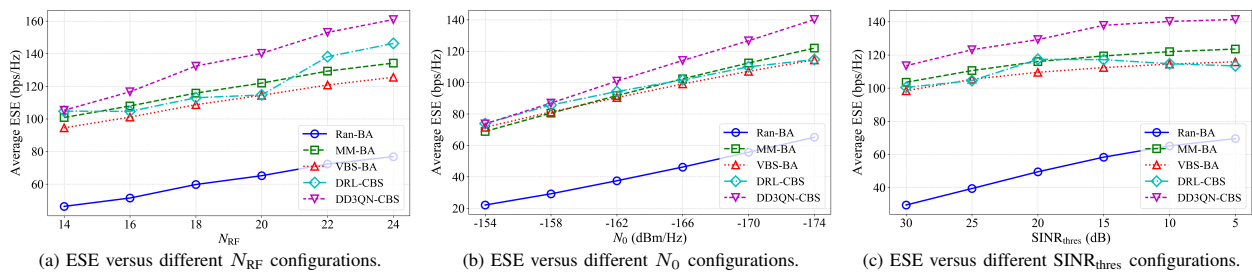


Fig. 6: ESE across different scenario configurations.

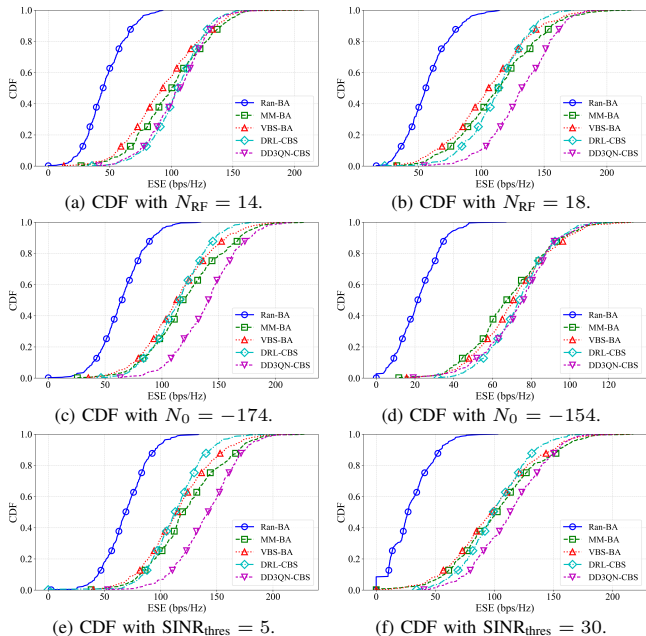


Fig. 7: CDF of test ESE under different configurations.

baseline [8]. This improvement is primarily attributed to the proposed action masking mechanism with the leader-follower strategy, which explicitly invalidates previously selected beams and thus prunes the exploration space at each time step. As a result, the agent can focus on optimizing valid beam combinations rather than learning to mitigate beam collisions. Across different configurations, the proposed algorithm consistently achieves higher training ESE values than the learning-based baseline, demonstrating its robustness and effectiveness in learning feasible beam selection policies.

## 2) Average ESE under Different Configurations

Fig. 6(a) evaluates the averaged ESE under different  $N_{RF}$  configurations. Increasing  $N_{RF}$  improves ESE because more RF chains allow more users to be served simultaneously and provide a larger BS-side beam selection space. The small gap between MM-BA and VBS-BA indicates that the VBS-assisted coarse beamspace representation can identify reliable candidate directions, while the gain of MM-BA comes from the VOP-based online measurement update. As  $N_{RF}$  increases, DD3QN-CBS achieves a larger gain over MM-BA because it learns joint BS-user beam assignments rather than ranking beams only by local gain. This allows DD3QN-CBS to better exploit additional RF-chain resources while avoiding highly correlated beam choices. In comparison, the performance fluctuation of DRL-CBS across different  $N_{RF}$  settings indicates its limited stability when the BS-side action

space changes.

Fig. 6(b) shows the impact of noise power density  $N_0$ . As the noise power increases, the ESE decreases for all schemes because fewer candidate links can satisfy the SINR constraint. The performance gap between DD3QN-CBS and MM-BA becomes smaller under stronger noise because many weak links are no longer usable, leaving fewer feasible beam combinations for the policy to optimize. Nevertheless, DD3QN-CBS consistently outperforms MM-BA because it can prioritize beam pairs that jointly balance link strength and inter-user separation, rather than relying only on the strongest individual beam gains.

Fig. 6(c) examines the effect of the QoS threshold  $SINR_{thres}$ . A stricter threshold reduces ESE because weak or highly interfered links are excluded from the feasible set. When the threshold is relaxed, more links become admissible, but the policy still needs to identify beam assignments that convert these feasible links into useful throughput. MM-BA cannot adapt beyond strongest-link ranking, while DRL-CBS shows non-monotonic behavior due to its penalty-dominated reward. The stable advantage of DD3QN-CBS indicates that the intermediate SINR-aware reward provides a smoother learning signal before the terminal ESE is observed.

## 3) Distribution of ESE under Different Configurations

Fig. 7 presents the cumulative distribution function (CDF) of the test ESE samples under different configurations.

Compared with Ran-BA, DRL-CBS improves the overall performance, but its penalty-based reward can bias the policy toward conservative collision avoidance and reduce exploration efficiency. This behavior tends to reduce the fraction of high-ESE samples in several configurations. In the lower-tail region, DD3QN-CBS achieves better performance by reducing poorly matched beam assignments, which improves the reliability of users that would otherwise dominate the outage events. In the high-ESE region, DD3QN-CBS remains comparable to MM-BA because the dominant beams in those samples are already well separated. The advantage of DD3QN-CBS therefore appears mainly as improved tail performance under difficult multi-user coupling conditions. Together with the average ESE results, the CDF analysis shows that the proposed framework also improves the reliability of coordinated beam selection.

## VI. CONCLUSION

In this paper, we proposed a VBS-guided beam management framework that leverages multi-modal environmental data to reduce beam training overhead and mitigate the MU-MIMO beam selection bottleneck in massive MIMO systems. The key idea is to model dominant single-bounce reflections through mirror symmetry across building facades recon-

structured from 3D LiDAR point clouds and location information, thereby constructing a compact VBS database without exhaustive wireless measurements. This database is mapped into a VBS-derived beamspace prior through coarse channel reconstruction, which guides VOP-based partial beam training with reduced online overhead. The calibrated measurements are then incorporated into a DD3QN-CBS algorithm. Simulation results on realistic urban layouts demonstrate improved beam training efficiency and beam selection performance over baseline methods. Moreover, the framework retains physical interpretability by explicitly representing dominant LoS and VLoS propagation opportunities through geometric mirror relations, suggesting that geometry-aware VBS representations can serve as a practical interface between multi-modal sensing data and interference-aware beam management. Future work can extend this framework to dynamic urban environments with moving blockers and online VBS database updates, and investigate lightweight reflection calibration to further improve the fidelity of VBS-derived beamspace priors.

#### REFERENCES

- [1] Y. Bian, W. Guo, J. Yang, S. Song, J. Zhang, S. Jin, and K. B. Letaief, "Multi-modal data driven virtual base station construction for massive MIMO beam alignment," in *Proc. IEEE Wireless Commun. and Netw. Conf. (WCNC)*, Apr. 2026, pp. 1–3.
- [2] K. B. Letaief, W. Chen, Y. Shi, J. Zhang, and Y.-J. A. Zhang, "The roadmap to 6G: AI empowered wireless networks," *IEEE Commun. Mag.*, vol. 57, no. 8, pp. 84–90, Aug. 2019.
- [3] F. Sahrabi and W. Yu, "Hybrid analog and digital beamforming for mmWave OFDM large-scale antenna arrays," *IEEE J. Sel. Areas Commun.*, vol. 35, no. 7, pp. 1432–1443, Jul. 2017.
- [4] T. Lin, J. Cong, Y. Zhu, J. Zhang, and K. Ben Letaief, "Hybrid beamforming for millimeter wave systems using the MMSE criterion," *IEEE Trans. Commun.*, vol. 67, no. 5, pp. 3693–3708, May 2019.
- [5] M. Giordani, M. Polese, A. Roy, D. Castor, and M. Zorzi, "A tutorial on beam management for 3GPP NR at mmWave frequencies," *IEEE Commun. Surveys Tuts.*, vol. 21, no. 1, pp. 173–196, 1st Quart. 2019.
- [6] Q. Xue, C. Ji, S. Ma, J. Guo, Y. Xu, Q. Chen, and W. Zhang, "A survey of beam management for mmWave and THz communications towards 6G," *IEEE Commun. Surveys Tuts.*, vol. 26, no. 3, pp. 1520–1559, 3rd Quart. 2024.
- [7] Z. Xu, S. Wang, and Y.-J. Angela Zhang, "Scenario-adaptive meta-learning for mmWave beam alignment," *IEEE Trans. Wireless Commun.*, vol. 24, no. 4, pp. 3192–3208, Apr. 2025.
- [8] Q. Hu, Y. Liu, Y. Cai, G. Yu, and Z. Ding, "Joint deep reinforcement learning and unfolding: Beam selection and precoding for mmWave multiuser MIMO with lens arrays," *IEEE J. Sel. Areas Commun.*, vol. 39, no. 8, pp. 2289–2304, Aug. 2021.
- [9] S. Jiang, G. Charan, and A. Alkhateeb, "LiDAR aided future beam prediction in real-world millimeter wave V2I communications," *IEEE Wireless Commun. Lett.*, vol. 12, no. 2, pp. 212–216, Feb. 2023.
- [10] A. Klautau, N. González-Prelcic, and R. W. Heath, "LiDAR data for deep learning-based mmWave beam-selection," *IEEE Wireless Commun. Lett.*, vol. 8, no. 3, pp. 909–912, 2019.
- [11] U. Demirhan and A. Alkhateeb, "Radar aided 6G beam prediction: Deep learning algorithms and real-world demonstration," in *Proc. IEEE Wireless Commun. and Netw. Conf. (WCNC)*, Austin, TX, USA, Apr. 2022, pp. 2655–2660.
- [12] G. Charan, M. Alrabeiah, T. Osman, and A. Alkhateeb, "Camera based mmWave beam prediction: Towards multi-candidate real-world scenarios," *IEEE Trans. Veh. Technol.*, vol. 74, no. 4, pp. 5897–5913, Apr. 2025.
- [13] Y. Feng, C. Zhao, F. Gao, Y. Zhang, and S. Ma, "Environment sensing-aided beam prediction with transfer learning for smart factory," *IEEE Trans. Wireless Commun.*, vol. 24, no. 1, pp. 676–690, Jan. 2025.
- [14] Y. Yang, F. Gao, X. Tao, G. Liu, and C. Pan, "Environment semantics aided wireless communications: A case study of mmWave beam prediction and blockage prediction," *IEEE J. Sel. Areas Commun.*, vol. 41, no. 7, pp. 2025–2040, Jul. 2023.
- [15] Y. Bian, J. Yang, S. Xia, and S. Jin, "3-D LiDAR and GPS aided beam tracking in millimeter wave vehicular communications," *IEEE Wireless Commun. Lett.*, vol. 13, no. 12, pp. 3290–3294, Dec. 2024.
- [16] H. Ahn, I. Orikumhi, J. Kang, H. Park, H. Jwa, J. Na, and S. Kim, "Machine learning-based vision-aided beam selection for mmWave multiuser MISO system," *IEEE Wireless Commun. Lett.*, vol. 11, no. 6, pp. 1263–1267, Jun. 2022.
- [17] K. Patel and R. W. Heath, "Harnessing multimodal sensing for multi-user beamforming in mmWave systems," *IEEE Trans. Wireless Commun.*, vol. 23, no. 12, pp. 18725–18739, Dec. 2024.
- [18] M. Farzanullah, H. Zhang, A. B. Sediq, A. Afana, and M. Erol-Kantarci, "Beam selection in ISAC using contextual bandit with multi-modal transformer and transfer learning," in *Proc. IEEE Int. Conf. Commun. Workshops (ICC Workshops)*, Jun. 2025, pp. 1978–1983.
- [19] R. T. Rakesh, G. Das, and D. Sen, "An analytical model for millimeter wave outdoor directional non-line-of-sight channels," in *Proc. IEEE Int. Conf. Commun. (ICC)*, May 2017, pp. 1–6.
- [20] C. E. O'Lone, H. S. Dhillon, and R. M. Buehrer, "Characterizing the first-arriving multipath component in 5G millimeter wave networks: TOA, AOA, and non-line-of-sight bias," *IEEE Trans. Wireless Commun.*, vol. 21, no. 3, pp. 1602–1620, Mar. 2022.
- [21] J. Yang, C.-K. Wen, and S. Jin, "Hybrid active and passive sensing for SLAM in wireless communication systems," *IEEE J. Sel. Areas Commun.*, vol. 40, no. 7, pp. 2146–2163, Jul. 2022.
- [22] S. Ganji, J. Kim, R. Sonigra, and P. R. Kumar, "TERRA: Beam management for outdoor mm-Wave networks," *IEEE Trans. Wireless Commun.*, vol. 23, no. 10, pp. 15112–15124, Oct. 2024.
- [23] M. Ester, H.-P. Kriegel, J. Sander, and X. Xu, "A density-based algorithm for discovering clusters in large spatial databases with noise," in *Proc. Int. Conf. Knowl. Discov. Data Min. (KDD)*, Portland, Oregon, USA, Aug. 1996, pp. 226–231.
- [24] H. Edelsbrunner and E. P. Mücke, "Three-dimensional alpha shapes," *ACM Trans. Graph.*, vol. 13, no. 1, pp. 43–72, 1994.
- [25] M. Garland and P. S. Heckbert, "Surface simplification using quadric error metrics," in *Proc. Annu. Conf. Comput. Graph. Interact. Tech. (SIGGRAPH)*, Aug. 1997, pp. 209–216.
- [26] T. Möller and B. Trumbore, "Fast, minimum storage ray-triangle intersection," *J. Graph. Tools*, vol. 2, no. 1, pp. 21–28, Aug. 1997.
- [27] R. J. Campello, D. Moulavi, A. Zimek, and J. Sander, "Hierarchical density estimates for data clustering, visualization, and outlier detection," *ACM Trans. Knowl. Discov. Data*, vol. 10, no. 1, pp. 1–51, Jul. 2015.
- [28] D. Wu, Y. Zeng, S. Jin, and R. Zhang, "Environment-aware and training-free beam alignment for mmWave massive MIMO via channel knowledge map," in *Proc. IEEE Int. Conf. Commun. Workshops (ICC Workshops)*, Montreal, QC, Canada, Jun. 2021, pp. 1–7.
- [29] X. Sun, C. Qi, and G. Y. Li, "Beam training and allocation for multiuser millimeter wave massive MIMO systems," *IEEE Trans. Wireless Commun.*, vol. 18, no. 2, pp. 1041–1053, Feb. 2019.
- [30] H. Kao, C.-Y. Wei, and V. Subramanian, "Decentralized cooperative reinforcement learning with hierarchical information structure," in *Proc. Int. Conf. Algorithmic Learn. Theory (ALT)*, S. Dasgupta and N. Hagh-talab, Eds., vol. 167, Apr. 2022, pp. 573–605.
- [31] Z. Wang, T. Schaul, M. Hessel, H. Hasselt, M. Lanctot, and N. Freitas, "Dueling network architectures for deep reinforcement learning," in *Proc. Int. Conf. Mach. Learn. (ICML)*, vol. 48, New York, New York, USA, Jun. 2016, pp. 1995–2003.
- [32] K. Fan, J. Zhang, X. Zhang, Y. Wu, J. Cao, Y. Zhou, and J. Ma, "Safety-polarized and prioritized reinforcement learning," in *Proc. Int. Conf. Mach. Learn. (ICML)*, vol. 267, Jul. 2025, pp. 15862–15886.
- [33] G. Varricchio, N. Alechina, M. Dastani, G. De Giacomo, B. Logan, and G. Perelli, "Pure-past action masking," in *Proc. AAAI Conf. Artif. Intell.*, vol. 38, no. 19, Feb. 2024, pp. 21646–21655.
- [34] T. Schaul, J. Quan, I. Antonoglou, and D. Silver, "Prioritized experience replay," 2016. [Online]. Available: <https://arxiv.org/abs/1511.05952>
- [35] C. Peel, B. Hochwald, and A. Swindlehurst, "A vector-perturbation technique for near-capacity multi-antenna multiuser communication-part i: channel inversion and regularization," *IEEE Trans. Commun.*, vol. 53, no. 1, pp. 195–202, Jan. 2005.
- [36] J. Hu, L. Shen, and G. Sun, "Squeeze-and-excitation networks," in *Proc. IEEE Conf. Comput. Vis. Pattern Recognit. (CVPR)*, Jun. 2018, pp. 7132–7141.
- [37] J. Hoydis, S. Cammerer, F. A. Aoudia, A. Vem, N. Binder, G. Marcus, and A. Keller, "Sionna: An open-source library for next-generation physical layer research," 2023. [Online]. Available: <https://arxiv.org/abs/2203.11854>
- [38] A. Sayeed and J. Brady, "Beamspace MIMO for high-dimensional multiuser communication at millimeter-wave frequencies," in *Proc. IEEE Global Commun. Conf. (GLOBECOM)*, Dec. 2013, pp. 3679–3684.